POLITECNICO DI TORINO
Repository ISTITUZIONALE

Functional Modifications Induced via X-ray Nanopatterning in TiO2 Rutile Single Crystals

Original
Functional Modifications Induced via X-ray Nanopatterning in TiO2 Rutile Single Crystals / Alessio, A.; Bonino, V.; Heisig, T.; Picollo, F.; Torsello, D.; Mino, L.; Martinez-Criado, G.; Dittmann, R.; Truccato, M.. - In: PHYSICA STATUS SOLIDI. RAPID RESEARCH LETTERS. - ISSN 1862-6254. - ELETTRONICO. - (2021), p. 2100409. [10.1002/pssr.202100409]

Availability:
This version is available at: 11583/2929177 since: 2021-10-05T14:47:40Z

Publisher:
John Wiley and Sons Inc

Published
DOI:10.1002/pssr.202100409

Terms of use:

This article is made available under terms and conditions as specified in the corresponding bibliographic description in the repository

Publisher copyright

(Article begins on next page)

02 May 2026

physica status solidi rrl
www.pss-rapid.com

Check for updates

Functional Modifications Induced via X-ray Nanopatterning in TiO_2 Rutile Single Crystals

*Andrea Alessio, Valentina Bonino, Thomas Heisig, Federico Picollo, Daniele Torsello, Lorenzo Mino, Gema Martinez-Criado, Regina Dittmann, and Marco Truccato**

The possibility to directly write electrically conducting channels in a desired position in rutile TiO_2 devices equipped with asymmetric electrodes—like in memristive devices—by means of the X-ray nanopatterning (XNP) technique (i.e., intense, localized irradiation exploiting an X-ray nanobeam) is investigated. Device characterization is carried out by means of a multitechnique approach involving X-ray fluorescence (XRF), X-ray excited optical luminescence (XEOL), electrical transport, and atomic force microscopy (AFM) techniques. It is shown that the device conductivity increases and the rectifying effect of the Pt/TiO_2 Schottky barrier decreases after irradiation with doses of the order of 10^{11} Gy and fluences of the order of 10^{12} J m^{-2}. Irradiated regions also show the ability to pin and guide the electroforming process between the electrodes. Indications are that XNP should be able to promote the local formation of oxygen vacancies. This effect could lead to a more deterministic implementation of electroforming, being of interest for production of memristive devices.

1. Introduction

Silicon-based electronics has recorded an exponential decrease for decades about the sizes of its basic components to achieve larger and larger integration scales and keep the pace of the so-called Moore's law. Nowadays, approaching the 7 nm technological node, the unavoidable process fluctuations create new challenges and require more and more sophisticated and expensive engineering solutions.[1] In this scenario, alternative approaches and novel device concepts are clearly desirable both to sustain further increase in the integration scale and to improve device functionality and performances. Oxide electronics has recently emerged as one of such promising approaches, having already been able to provide monolithic full-oxide integrated circuits, for instance.[2] But the advent of this new oxide-based technology has also opened the way to the fabrication of conceptually new devices like memristors,[3] i.e., resistive devices with inherent memory properties that previously existed just as theoretical models. Since then, memristor-based electronics has seen a rapid progress and showed great potential for many applications spanning from neuromorphic computing to on-chip memory and storage.[4–6] These devices are typically based on the reversible change of the electrical properties of transition metal oxides upon the application of an electric field that causes the introduction and migration of oxygen vacancies, which act as mobile donors in these systems. The typical two-terminal device structure of memristors consists of a dielectric layer of a material like TiO_2, $SrTiO_3$, or HfO_2 placed between two metallic electrodes. Prior to the reversible operation of the devices, a voltage

A. Alessio, F. Picollo, M. Truccato
Department of Physics, Interdepartmental Centre NIS
University of Torino
via P. Giuria 1, I-10125 Torino, Italy
E-mail: marco.truccato@unito.it

V. Bonino
European Synchrotron Radiation Facility – Experiments Division
71 Avenue des Martyrs, F-38000 Grenoble, France

T. Heisig, R. Dittmann
Forschungszentrum Juelich GmbH
Peter Gruenberg Institute 7, D-52425 Juelich, Germany

The ORCID identification number(s) for the author(s) of this article can be found under https://doi.org/10.1002/pssr.202100409.

© 2021 The Authors. physica status solidi (RRL) Rapid Research Letters published by Wiley-VCH GmbH. This is an open access article under the terms of the Creative Commons Attribution License, which permits use, distribution and reproduction in any medium, provided the original work is properly cited.

DOI: 10.1002/pssr.202100409

T. Heisig, R. Dittmann
JARA-FIT
RWTH Aachen University
D-52056 Aachen, Germany

D. Torsello
Department of Applied Science and Technology
Politecnico di Torino
10129 Turin, Italy

D. Torsello
Istituto Nazionale di Fisica Nucleare
Sezione di Torino, 10125 Turin, Italy

L. Mino
Department of Chemistry, Interdepartmental Centre NIS and INSTM
Centro di Riferimento
University of Torino
via P. Giuria 7, I-10125 Torino, Italy

G. Martinez-Criado
Instituto de Ciencia de Materiales de Madrid
Consejo Superior de Investigaciones Científicas
28049 Cantoblanco, Spain

© 2021 The Authors. physica status solidi (RRL) Rapid Research Letters published by Wiley-VCH GmbH

exceeding the usual switching voltage has to be applied in order to turn the highly insulating dielectric layers into a switchable state. This so-called electroforming process comprises complex electronic and ionic processes,[7] often mediated by Joule heating and thermal runaways, and results in a release of oxygen from the lattice and the formation of oxygen vacancies along one[8,9] or several nanosized filaments.[10] During subsequent switching, the device resistance changes when proper voltage pulses are applied and move the oxygen vacancies, establishing or interrupting conducting filaments between the electrodes, which can be associated to two different logical states.[11] One of the major problems hindering large-scale diffusion of these devices is represented by the highly stochastic nature of the filament formation, which leads to a large variability of the performances from device to device and even from cycle to cycle for the same device. The size of the filament can be influenced by the electroforming conditions such as forming voltage and current compliance.[12,13] However, the size, shape, and position of the filaments might change upon cycling and thereby cause cycle-to-cycle variations.[14] Therefore, different approaches have been used to pinpoint the filament position by means of modifications of the material stack that locally enhance the electric field, such as embedding nanoparticles into the electrode[15] or the dielectric film,[16,17] or using pyramidal-shaped electrodes.[18] Moreover, methods to confine the ionic motion by providing holes in an oxygen-blocking graphene interlayer[19] and by fabricating nanocavities along misfit dislocations[20] have been used to guide the ionic filament formation process.

In addition to the stochasticity of the filament formation, the need of an electroforming process in filamentary memristors has additional drawbacks with respect to circuit design and power consumption. In particular, the need to form all devices with a higher voltage prior to the circuit operation is a time- and energy-consuming step that strongly limits the circuit design flexibility and increases the power consumption. In this sense, the ability to replace the electroforming step and to develop methods to control the formation and ordering of oxygen vacancies in memristive oxides by other means would represent a great step toward large-scale production and application of memristors.

Some steps in the direction of inducing a localized, controlled amount of oxygen vacancies have already been moved in the field of superconducting oxides. Indeed, some of us have already shown that, using synchrotron radiation nanoprobes with sizes of the order of $50 \times 50\,nm^2$ and modifying the corresponding photon flux and dose, it is possible to switch from ordinary material characterization to material modification.[21–27] In the case that a superconducting oxide is irradiated in an approximately uniform way, this treatment corresponds to a variation of its oxygen doping level,[28–30] but if only some carefully designed portions are irradiated, a current path can be drawn in the material in such a way to fabricate a Josephson device.[31]

Thus, the whole technique can be considered an alternative X-ray nanopatterning (XNP) method to locally introduce defects in oxides and fabricate devices as desired without etching the crystals. Actually, the microscopic mechanism responsible for these material modifications is not clear yet. Careful space- and time-resolved numerical simulations of the interaction between the superconducting oxides and the X-ray nanobeam have shown that ordinary melting must be excluded,[32] leaving room for thermal fatigue or marginal non-thermal melting as two possible candidates (see also Supporting Information).[33–36] Nevertheless, the first indications that this mechanism could be relevant also for a transition metal oxide like TiO_2 were reported in the past for $Pt/TiO_2/Pt$ cells, where it was shown that prolonged, nonspatially controlled synchrotron irradiation acting in synergy with an applied DC electric field was able to induce structural changes corresponding to oxygen depletion and transition to the Ti_4O_7 Magneli phase.[37] Following these indications, we have applied the XNP method to nonannealed TiO_2 rutile single crystals with two Au electrodes and shown that controlled irradiation can open a subsurface conduction channel in the insulating region between two electrodes.[38] This experiment proved that XNP can be applied also to materials where the binding energy for oxygen is much greater than the one corresponding to the interstitial atoms present in the superconducting oxides. However, we were neither able to prove the ability of XNP to locate and pin the formation of conducting channels nor to observe which kind of changes could be associated in our case to the device-resistance transition. This is the problem this article is intended to face.

2. Experimental Section

The devices were fabricated by depositing two metal electrodes on a (110)-oriented TiO_2 rutile single crystal. The corresponding geometry is shown in **Figure 1**b. One electrode was made of Pt (60 nm in thickness), whereas the other one was made by depositing 30 nm of Pt on top of 30 nm of Ta (Figure 1c). Two sizes of the gap between the electrodes were used during the experiments, about 1.9 and 6.7 μm in width, respectively. The samples with a 1.9 μm gap were annealed at 300 °C in H_2/Ar (4%) atmosphere for 2 h. This annealing procedure was strongly reducing and was expected to cause the formation of oxygen vacancies in rutile and thereby to increase the sample electronic conductivity. A temperature as low as 300 °C was selected to minimize the change of the surfaces and interfaces of the electrodes. However, as the oxygen exchange reaction was strongly kinetically limited at this temperature and due to the lack of reference studies in this temperature range, it was impossible to accurately predict the oxygen vacancy concentration caused by this annealing step. Based on extrapolations from

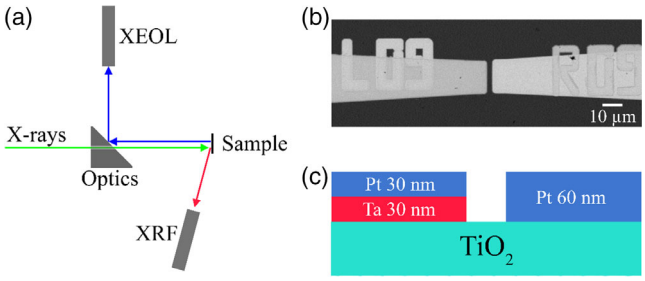

Figure 1. a) Sketch of the experimental setup used at beamline ID16B (XRF represents the X-ray fluorescence detector, XEOL indicates the X-ray excited optical luminescence detector). b) Scanning electron microscopy (SEM) image of a typical sample (top view) and c) schematic cross section.

© 2021 The Authors. physica status solidi (RRL) Rapid Research Letters published by Wiley-VCH GmbH

1000 to 300 °C,[39] one can regard $x = 10^{-5}$ as the upper limit for the oxygen deficiency in TiO_{2-x}. In addition to this, additional oxygen vacancies were caused at the Ta/TiO_2 interface due to the formation of a Ta_2O_{5-x} interface layer.[40] The Pt electrode was expected to form a Schottky barrier with rutile, resulting in a rectifying effect for the devices, whereas the Ta one formed an ohmic contact. This provided the asymmetry generally needed to observe bipolar resistive switching.[41]

X-ray characterization and irradiation sessions were carried out during two subsequent experimental campaigns at the nanoprobe beamline ID16B of the European Synchrotron Radiation Facility (ESRF) in Grenoble, France.[42] The first campaign took place before the ESRF upgrade to the new fourth generation of synchrotron light sources, which has been named as extremely brilliant source (EBS), whereas the second campaign was scheduled after the upgrade. In both cases, the X-ray beam was focused by means of Kirkpatrick–Baez mirrors into a spot size of the order of $50 \times 50\,nm^2$ and the experimental setup consisted of an optical microscope for preliminary sample alignment, a X-ray fluorescence (XRF) detector and a X-ray excited optical luminescence (XEOL) system equipped with a high numerical aperture collection optics, whose axis coincides with the X-ray nanobeam. Devices were mounted on a customized sample holder with electrical connections, which also allowed to carry out 2-probe electrical characterizations between subsequent irradiation sessions without removing the sample from the beamline.

As a typical procedure for characterization before irradiation of all the devices, a preliminary localization of the gap was obtained through an optical microscope, and the subsequent acquisition of XRF maps allowed a precise localization of the metal electrodes. Simultaneous XRF and XEOL characterization maps were acquired by raster scanning the sample area of interest in the X-ray nanobeam, after inserting Si filters to reduce the photon flux to avoid unwanted material modifications. Elemental maps were obtained by fitting the collected XRF spectra with the PyMCA code[43] using the X-ray emission lines of the elements present in the samples (Ti, Pt, and Ta), together with Ar and Kr from the atmosphere and some expected impurities in rutile crystals (Sr, Y, Si, and Fe).

After electrical characterization of their pristine state, devices were irradiated by scanning the samples across the X-ray nanobeam along lines connecting the two metal electrodes. The details of the irradiation procedure were different for the two experimental campaigns. The nonannealed samples with a 6.7 μm gap were irradiated during the first campaign with a $55 \times 52\,nm^2$ nanobeam, with an energy of 17.8 keV in pink beam mode ($\Delta E/E \approx 10^{-2}$) and the 16-bunch filling mode of the storage ring, corresponding to a maximum current of 90 mA. This filling mode consisted of a train of 16 equally spaced, equally highly populated electron bunches rotating in the storage ring, each of them generating a current equal to 90 mA/16 bunch = 5.6 mA/bunch. These bunches originated X-ray pulses with a Gaussian time profile with a rms duration $RMS_t \approx 48$ ps and separated by $t_{sep} = 1.76 \times 10^{-7}$ s from each other. A single line connecting the two electrodes was irradiated multiple times with a 50 nm step at increasing exposure times and photon fluxes by progressively removing Si filters from the beam, up to a maximum time-averaged photon flux $\Phi_0 = 1 \times 10^{11}\,ph\,s^{-1}$. In this 16-bunch filling mode, such a maximum value of Φ_0 corresponds to about 1.76×10^4 photons per pulse and to a fluence of $1.76 \times 10^4\,J\,m^{-2}$ per pulse (see Supporting Information). At the pulse repetition rate of $1/t_{sep} = 5.68 \times 10^6\,s^{-1}$, the exposure times used during the whole experiment corresponded to a total cumulative dose $CD = 7.51 \times 10^{11}$ Gy and to a total cumulative fluence of $CF = 1.70 \times 10^{12}\,J\,m^{-2}$. After each irradiation step, a current–voltage characteristic (i.e., a so-called *IV* curve) was also recorded. The annealed samples with a 1.9 μm gap were irradiated during the second campaign with a $57 \times 59\,nm^2$ beam with an energy of 17.5 keV in pink beam mode and 7/8 + 1 filling mode of the storage ring. This mode consisted in filling 7/8 of the storage ring length with 868 equally spaced bunches of about 0.23 mA/bunch, having at their extremes two bunches of 1 mA. The remaining 1/8 of the storage ring was filled in its center by a single bunch of 2 mA. This resulted in a typical rms duration of the pulses $RMS_t \approx 20$ ps, with a separation time between the 0.23 mA bunches equal to 2.84×10^{-9} s and another separation time of 1.76×10^{-7} s between the 1 and the 2 mA bunches. In this campaign, as a first step, an area of $6.8 \times 1\,\mu m^2$ was irradiated, with a 200 nm step size for the mesh in both directions, in such a way so as to connect the two metal electrodes. This irradiation pattern was repeated multiple times at increasing photon fluxes and exposure times, up to a maximum time-averaged flux $\Phi_0 = 4 \times 10^{12}\,ph\,s^{-1}$ and a maximum exposure time of 5 s per point. In the 7/8 + 1 filling mode, this maximum value of Φ_0 corresponded to about 1.12×10^5 photons forming the largest X-ray pulse, i.e., the one generated by the 2 mA bunch, which produced a fluence of $9.38 \times 10^4\,J\,m^{-2}$ per each of these pulses (see Supporting Information). As a second step, a single line was irradiated in the same region, with maximum photon flux and 25 s per point. This corresponded to a total cumulative dose, $CD = 2.4 \times 10^{13}$ Gy and to a total cumulative fluence, $CF = 5.3 \times 10^{13}\,J\,m^{-2}$. *IV* curves were also acquired between irradiations.

Then, after both irradiation and electrical characterization, XRF and XEOL maps were simultaneously acquired once more. At the end of each campaign, samples were also analyzed by means of conducting atomic force microscopy (C-AFM) with a Cypher S system by Asylum Research available at the Partnership for Soft Condensed Matter (PSCM) of ESRF.

3. Results and Discussion

Figure 2a–c shows representative XRF elemental maps corresponding to Pt–L, Ta–L, and Ti–K lines, respectively, for a pristine sample. Samples from both experimental campaigns invariably show the same features: a sample from the second experimental campaign is shown in Figure 2 for the ease of comparison with the following.

It is possible to observe a smaller Pt signal on the left electrode, which corresponds to the Pt/Ta electrode, due to the lower amount of Pt compared with the right electrode. This is confirmed by the Ta map, where only the left electrode is visible, as expected. In contrast, the Ti–K signal shows a lower intensity in correspondence with the two electrodes. Keeping in mind that at 17.5 keV the attenuation length in TiO_2 is over 160 μm, this result can be ascribed to a shadow effect of the metal electrodes partially absorbing the XRF signal coming from the bulk of the substrate underneath.

© 2021 The Authors. physica status solidi (RRL) Rapid Research Letters published by Wiley-VCH GmbH

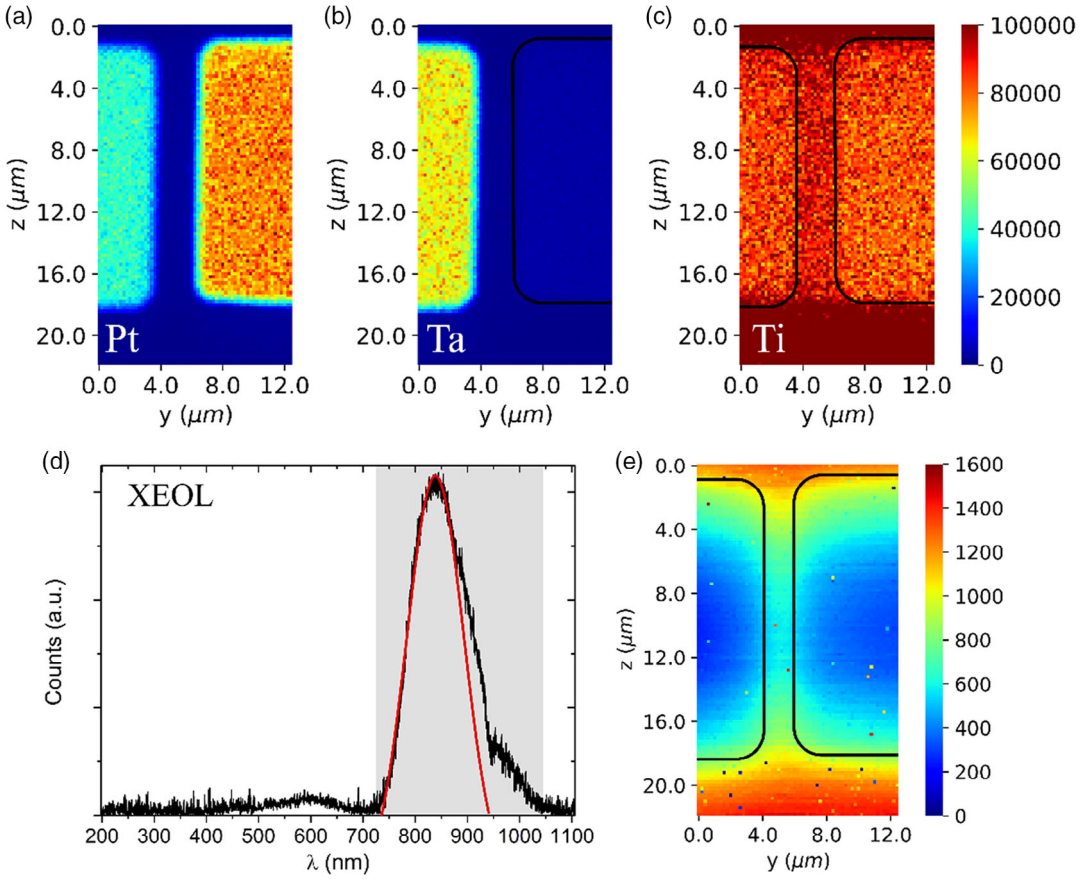

Figure 2. a–c) XRF maps corresponding to Pt–L lines (a), Ta–L lines (b), and Ti–K lines (c) collected from a typical pristine sample. d) XEOL spectrum integrated over the whole scanning area. The red curve highlights the main Gaussian contribution to the spectrum in the NIR region (shaded area). e) XEOL map corresponding to the intensity of the main Gaussian contribution of (d). The black solid lines in (b), (c), and (e) represent the metal electrode contours.

The corresponding XEOL spectrum integrated over the whole scanning sample area is shown in Figure 2d. It shows a broad emission component in the near infrared region with a maximum located around $\lambda = 830$ nm, corresponding to a photon energy $E = hc/\lambda = 1.49$ eV. Similar photoluminescence spectra have already been reported for rutile single crystals[44–46] and have been attributed to the radiative recombination of electrons trapped in a midgap state with free holes in the valence band.[45] This midgap state, located about 1.5 eV below the conduction band edge, in principle could be related both to the presence of interstitial Ti atoms[45] and to the presence of oxygen vacancies inducing the reduction of Ti^{4+} to Ti^{3+}.[47] However, the study of the temperature dependence of photoluminescence spectra in rutile has pointed out the importance of oxygen vacancies in trapping the carriers at low temperature ($T = 20$ K) and in producing a discrete set of lines, which are smoothed over and transformed into a continuous spectrum at higher temperatures ($T \geq 100$ K) due to the increasing mobility of the carriers.[44] Therefore, experimental indications are in favor of oxygen vacancies as the origin of the midgap state in rutile.

The XEOL spectrum was fitted with multiple Gaussian contributions, obtaining the spatial distributions of the three parameters defining each Gaussian curve (height, full width at half maximum, and wavelength of the maximum). In Figure 2e, the map corresponding to the height of the main Gaussian contribution located around 830 nm is reported as the most informative one. A significant decrease in the intensity can be observed in the location of the metal electrodes, due to a screening effect by the metal electrodes analogous to what observed for the XRF signal.

3.1. First Experimental Campaign

Figure 3 shows the current I versus electric field E curves obtained during the first experimental campaign after each irradiation for a nonannealed sample (6.7 μm gap). A clear increase in the sample conductivity is observed with increasing the irradiation dose, along with the appearance of a hysteresis. This hysteresis can be considered as related to trapping of carriers at trap levels,[48,49] which creates a spatial charge distribution and induces an electric counter field, leading to a decrease in the device conductivity with time. The typical timescale observed for the current decrease at constant E value is of the order of 10–100 s (see Supporting Information). Therefore, upon increasing and subsequently decreasing E during acquisition of the IV curves, current values corresponding to the same E values progressively decrease, inducing the appearance

© 2021 The Authors. physica status solidi (RRL) Rapid Research Letters published by Wiley-VCH GmbH

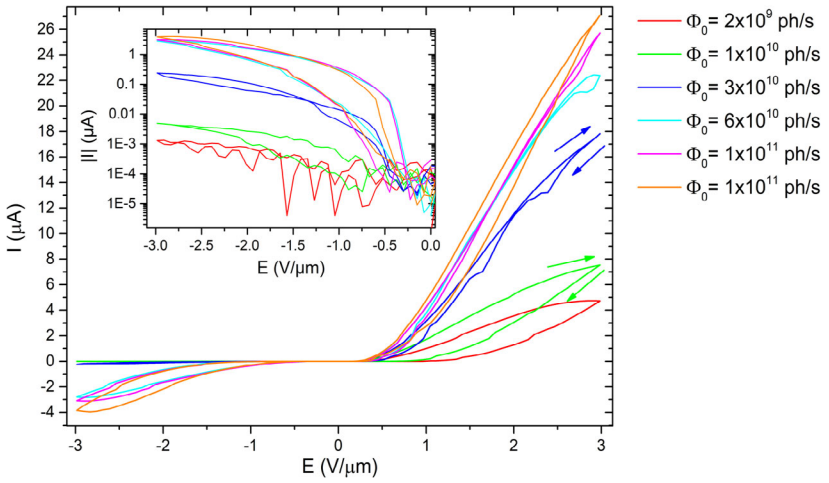

Figure 3. *I* versus *E* curves after multiple irradiations at increasing time-averaged photon fluxes, measured for a first-campaign sample (nonannealed, 6.7 μm gap). The exposure time was 1 s per point for each irradiation, except for the last one corresponding to the orange curve, whose exposure time was increased to 10 s per point. Cumulative doses correspond to CD = 1.96×10^9 (red), 1.19×10^{10} (green), 4.25×10^{10} (blue), 1.03×10^{11} (cyan), 2.03×10^{11} (magenta), and 7.51×10^{11} (orange) Gy, and cumulative fluences to CF = 4.43×10^9 (red), 2.70×10^{10} (green), 9.60×10^{10} (blue), 2.33×10^{11} (cyan), 4.59×10^{11} (magenta), and 1.70×10^{12} (orange) J m^{-2}. The inset shows the absolute value of the current of the negative branch in a logarithmic scale.

of a hysteresis (see arrows in Figure 3). Moreover, the rectifying effect due to the Schottky barrier between rutile and Pt becomes less pronounced with increasing irradiation, with a remarkable increase in the reverse current by at least three orders of magnitude (see inset of Figure 3).

Analogous hysteretic behaviors were recently reported for instance in ZrO_x memristors, with a practically identical timescale for the current decay.[50] These features were explained by means of a microscopic model where donor-type traps are located close to the interface between the oxide and the Pt electrode. The energy of these trap levels lies in the energy gap below the Fermi level and shows a continuous distribution about 1 eV wide. During the acquisition of the *IV* curves, these trap levels get charged, slightly changing their energy position in the gap and generating a space charge which also affects the height and width of the Schottky barrier. Such a model can also explain the behavior of the irradiated samples shown in Figure 3, provided that we identify the donor-type trap levels with nonmobile oxygen vacancies located under the Pt electrode.

After irradiation and electrical characterization, topographic and C-AFM images were collected as well. In **Figure 4**a, the topographic signal from AFM is reported, showing a morphological trace in correspondence with the irradiation line with a maximum height of about 14 nm. This feature could be explained in terms of a chemical expansion of the rutile unit cell because of the local increase in the density of oxygen vacancies.[51] Moreover, the C-AFM image reported in Figure 4b clearly shows at the same position an electrically conducting path induced by the X-ray irradiation, which extends up to the surface of the sample and testifies that TiO_2 has been locally turned into a conducting material. This behavior further supports the hypothesis of a local increase in the density of oxygen vacancies and significantly differs with respect to previous XNP experiments carried out on rutile single crystals with two Au electrodes, where no evident change

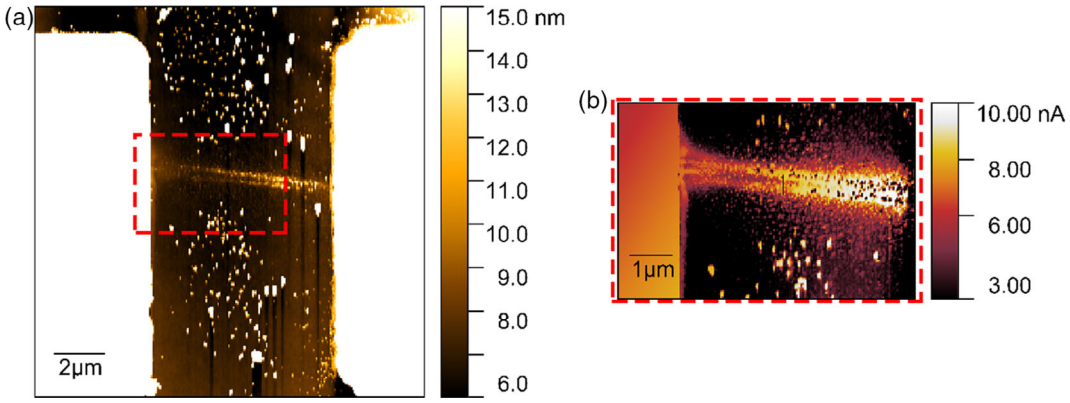

Figure 4. a) Topographic and b) C-AFM images of a gap after irradiation of a first-campaign sample (nonannealed, 6.7 μm gap).

© 2021 The Authors. physica status solidi (RRL) Rapid Research Letters published by Wiley-VCH GmbH

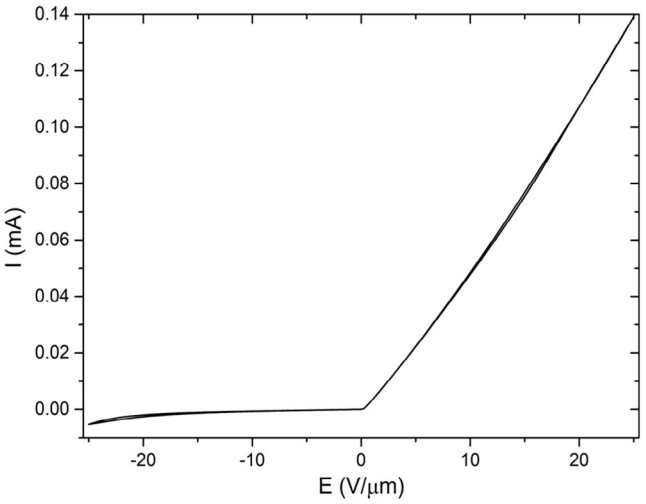

Figure 5. *I* versus *E* curve of a second-campaign sample (annealed, 1.9 μm gap) before irradiation.

in surface conductivity was highlighted after irradiation.[38] This was attributed to the formation of subsuperficial conductive channels. By comparing these two experiments, we can observe that in the present case, the use of an ohmic electrode (i.e., Ta) has resulted in a direct-polarization current in the *IV* curves that is one order of magnitude larger than the previous one. Most likely, such a more intense current has induced a more significant heating of the conduction channel, with a corresponding higher mobility and higher concentration of the oxygen vacancies on the surface, which has allowed them to be detected by C-AFM. However, these data are not enough to discriminate whether a similar concentration of oxygen vacancies was already present on the surface after the XNP irradiation, excluding any significant influence of the bias applied to measure the *IV* curves.

3.2. Second Experimental Campaign

To try to obtain the resistive switching, we changed many experimental parameters and moved to annealed samples in which a higher concentration of oxygen vacancies was induced by the treatment in H_2 atmosphere (see Experimental Section). We also used a shorter gap (1.9 μm) to achieve higher electric field values. In **Figure 5**, a typical *I* versus *E* curve of a pristine device of the second campaign is reported. It is possible to see that before irradiation these samples show a clear rectifying behavior and no hysteresis, even for *E* values considerably higher than the ones shown in Figure 3.

After irradiation with $CD = 2.4 \times 10^{13}$ Gy and $CF = 5.3 \times 10^{13}$ J m^{-2}, *I* versus *E* curves were acquired by progressively increasing the maximum *E* value (see **Figure 6**a). Once again, a hysteresis can be observed, especially in the positive branch, corresponding to a less rectifying behavior with respect to the one of pristine samples. By further increasing the maximum *E* value, an electroforming process takes place (see Figure 6b), as testified by the sudden increase in the current up to the compliance value of the voltage source (≈2.5 mA).

Subsequently, some *I* versus *E* curves were acquired with a lower maximum value for *E*, and all of them corresponded to a low-resistance state (the so-called "on" state, see the green curve in Figure 6b), confirming a nonvolatile change in the device resistance. Despite many attempts to reverse the device behavior back to its pristine high-resistance state were made, no more transition was observed.

XRF and XEOL maps were then acquired for these samples around the irradiated region after device electroforming, with a typical step size of 200 nm in both directions. They are shown in **Figure 7**. From the Pt–L and Ta–L line maps (Figure 7a,b), it is clear that the Pt electrode was partially damaged as a consequence of the sudden discharge during the onset process, whereas the Ta/Pt electrode remained unchanged. We can also

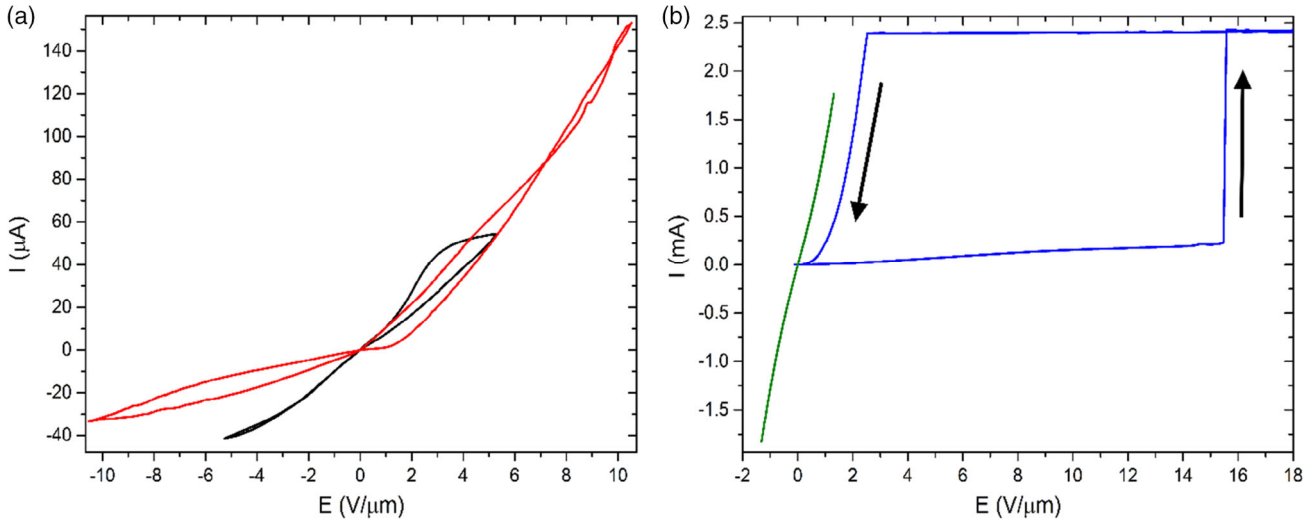

Figure 6. a) *I* versus *E* curves measured for a second-campaign sample (annealed, 1.9 μm gap) after irradiation with $CD = 2.4 \times 10^{13}$ Gy and $CF = 5.3 \times 10^{13}$ J m^{-2}, at increasing maximum voltages. b) *I* versus *E* curve showing the electroforming process (blue) and subsequent *I* versus *E* curve in the so-called "on" state (green).

© 2021 The Authors. physica status solidi (RRL) Rapid Research Letters published by Wiley-VCH GmbH

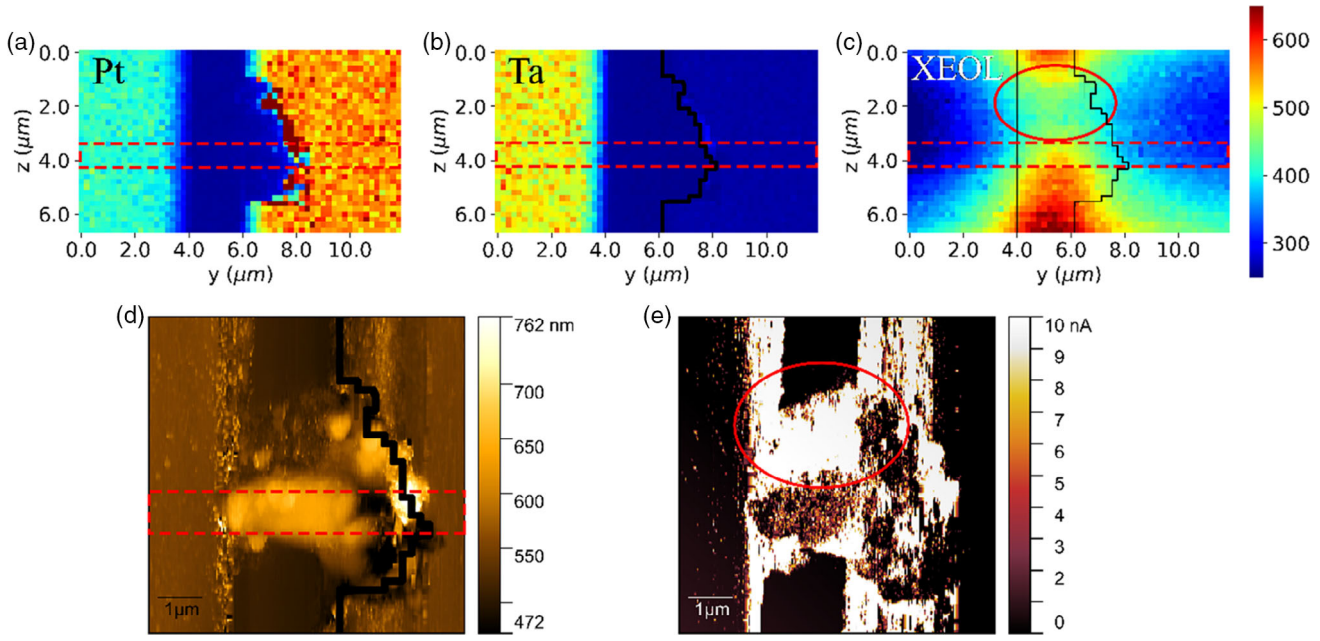

Figure 7. a,b) Typical XRF maps collected for a second-campaign sample (annealed, 1.9 μm gap) after irradiation and electroforming, corresponding to Pt–L (a) and Ta–L (b) lines. c–e) Corresponding XEOL (c), topographic (d), and C-AFM (e) images after irradiation and electroforming are also displayed. The dashed red boxes highlight the irradiated region, and the solid red circles indicate the minimum in the XEOL (c) and the maximum in the C-AFM (e) signals.

observe the absence of metal traces inside the gap, which excludes the possibility of electromigration of metal electrode ions such as Pt or Ta as an explanation for the onset of the low-resistance state of the device.

An AFM image was also acquired after electroforming and is shown in Figure 7d. It is possible to see a morphological bump about 150 nm in height that is centered on the irradiated line and that is also in correspondence with the damaged portion of the electrode. The device polarization (positive Pt vs negative Ta/Pt) and the asymmetrical shape of the bump are in agreement with the scenario of the thermally enhanced oxygen vacancy assembly for the electroforming process, where irregularities of the cathode can result in high values of the local current density, and therefore, induce a remarkable increase in the local temperature due to the Joule effect. This local heating facilitates the drift of oxygen ions under the action of the strong electric field, leading to the accumulation of oxygen vacancies near the cathode and to the growth of the oxygen vacancy filament from the cathode toward the anode.[52–54] It can also be observed that the bump shows a rounded shape and droplet-like structures around it, which could be considered as an indication of possible local melting to have occurred during the electroforming, further confirming the involvement of significant local Joule heating in the process. Moreover, this oxygen vacancy assembly scenario also implies the migration of oxygen ions and their release at the Pt anode, which explains the local delamination of this electrode.

On the whole, position and structure of the electroformed bump represent an evidence that XNP can provide the sample irregularities necessary to start and guide the electroforming process in the desired position, probably because of the large local density of oxygen vacancies induced in the nanobeam track. Apparently, this process made the switch to the "on" state for the conducting channel irreversible, but at the same time indicates that a possible strategy to obtain a reversible resistance transition could be represented by the use of lower current compliances in order to accurately modulate the local heating intensity and, consequently, the migration of oxygen vacancies and the filament size.

Figure 7c shows the XEOL signal collected over the same area as the XRF maps. Again, a lower intensity can be observed in correspondence with the two electrodes, as expected. Also, the luminescence intensity in the gap region was expected to be consistent with the XEOL maps acquired before electroforming, i.e., practically constant over the 6 μm vertical scale of Figure 7c. On the contrary, it is possible to observe a ≈30% modulation of the XEOL signal, with a lower intensity in the region highlighted by the solid red circle, which is close to but does not correspond exactly to the irradiated portion of the sample (dashed red lines). Moreover, it is also possible to observe that the C-AFM image reported in Figure 7e shows a higher conductivity region on the border of the bump, which corresponds to the same position as the low intensity area of the XEOL signal.

A possible explanation for these two observations could be represented by the presence of a high density of oxygen vacancies in this region of the device, which induces a variety of electronic states located within 0.7 eV from the bottom of the conduction band.[47,55] Indeed, on one hand, this situation would offer nonradiative recombination paths to photoexcited electrons, which results in a local decrease in the luminescence signal.[45] On the other hand, it could increase the surface conductivity because of thermally excited electrons coming from these defective states, which could be considered as shallow donor levels for the conduction band and that can also affect the overall band structure at the rutile/metal Schottky barrier in such a way to favor the

© 2021 The Authors. physica status solidi (RRL) Rapid Research Letters published by Wiley-VCH GmbH

injection of mobile carriers, similarly to what has already been proved in $SrTiO_3$ and in ZrO_x.[50,56]

4. Conclusion

We have pursued a global picture of the phenomena occurring during XNP of memristive devices by carrying out a multitechnique investigation (XRF, XEOL, *IV* curves, AFM). We have shown that it is possible to open conducting microchannels in insulating TiO_2 rutile single crystals by means of local X-ray irradiation with typical doses of the order of 10^{11} Gy and fluences of the order of 10^{12} J m^{-2}. This phenomenon consists both in an increase in the electrical conductivity and in a decrease in the rectifying effect of the Schottky barrier between rutile and the Pt contact, in agreement with an increase in the oxygen vacancy donor concentration in the space charge region. Moreover, these microchannels have shown the ability to locate and guide the electroforming process between the electrodes, most likely involving intense local Joule heating but no atomic migration of the metal electrodes. Indications are that the formation of oxygen vacancies should probably be promoted by XNP on a local basis, and that the electroforming process could subsequently rearrange their position into continuous highly conductive regions that also act as nonradiative recombination centers for electrons, although experimental evidences to support this picture are not conclusive yet.

These results could be interesting from the point of view of the production technology of memristive devices, as they could pave the way toward a more reliable and deterministic performances of electroforming. However, the nature of the structural defects induced by irradiation and the corresponding microscopic mechanisms responsible for their formation are presently unclear and call for further investigations to fully exploit the potential of this method. Of course, this would also imply an optimization of the process parameters to avoid excessive local heating and to achieve a reversible resistance switching.

Supporting Information

Supporting Information is available from the Wiley Online Library or from the author.

Acknowledgements

The authors thank F. Gunkel for helpful discussions and support with the annealing of the rutile crystals. The authors also thank the ESRF for allocation of beamtime at the beamline ID16B, for AFM support at the Partnership for Soft Condensed Matter (PSCM), and for the kind availability of all of its staff. A.A., F.P., and M.T. also acknowledge partial support from the "Departments of Excellence" (L. 232/2016) grant, funded by the Italian Ministry of Education, University and Research (MIUR). T.H. and R.D. were supported by the DFG (German Science Foundation) within the collaborative research center SFB 917 "Nanoswitches." G.M.-C. acknowledges the funding by the Spanish Ministry of Innovation, Science, and Technology and the Spanish Ministry of Economy through Research Project RTI2018-097195-B-I00. In addition, the funding from European Union QUANTIMONY project within Horizon 2020 MSCA research and innovation programme under grant agreement no. 860110 is acknowledged.

Open Access Funding provided by Universita degli Studi di Torino within the CRUI-CARE Agreement.

Conflict of Interest

The authors declare no conflict of interest.

Data Availability Statement

The data that support the findings of this study are available from the corresponding author upon reasonable request.

Keywords

electroforming, memristors, oxygen vacancies, TiO_2, X-ray nanopatterning

Received: July 27, 2021
Revised: September 1, 2021
Published online:

[1] M. Anees, K. Rahul, S. A. Swarnkar, S. Yachareni, in *IEEE 14th Dallas Circuits and Systems Conf. (DCAS)*, IEEE, Piscataway, NJ **2020**, https://doi.org/10.1109/DCAS51144.2020.9330648.
[2] R. Jany, C. Richter, C. Woltmann, G. Pfanzelt, B. Forg, M. Rommel, T. Reindl, U. Waizmann, J. Weis, J. A. Mundy, D. A. Muller, H. Boschker, J. Mannhart, *Adv. Mater. Interfaces* **2014**, *1*, 1300031.
[3] D. B. Strukov, G. S. Snider, D. R. Stewart, R. S. Williams, *Nature* **2008**, *453*, 80.
[4] R. Dittmann, J. P. Strachan, *Appl. Mater.* **2019**, *7*, 110903.
[5] D. Ielmini, *Semicond. Sci. Technol.* **2016**, *31*, 063002.
[6] M. A. Zidan, J. P. Strachan, W. D. Lu, *Nat. Electron.* **2018**, *1*, 22.
[7] A. A. Sharma, I. V. Karpov, R. Kotlyar, J. Kwon, M. Skowronski, J. A. Bain, *J. Appl. Phys.* **2015**, *118*, 114903.
[8] J. J. Yang, M. D. Pickett, X. M. Li, D. A. A. Ohlberg, D. R. Stewart, R. S. Williams, *Nat. Nanotechnol.* **2008**, *3*, 429.
[9] D. H. Kwon, K. M. Kim, J. H. Jang, J. M. Jeon, M. H. Lee, G. H. Kim, X. S. Li, G. S. Park, B. Lee, S. Han, M. Kim, C. S. Hwang, *Nat. Nanotechnol.* **2010**, *5*, 148.
[10] H. C. Du, C. L. Jia, A. Koehl, J. Barthel, R. Dittmann, R. Waser, J. Mayer, *Chem. Mater.* **2017**, *29*, 3164.
[11] S. Kim, S. Choi, W. Lu, *ACS Nano* **2014**, *8*, 2369.
[12] Z. Wei, T. Takagi, Y. Kanzawa, Y. Katoh, T. Ninomiya, K. Kawai, S. Muraoka, S. Mitani, K. Katayama, S. Fujii, R. Miyanaga, Y. Kawashima, T. Mikawa, K. Shimakawa, K. Aono, in *2011 Int. Electron Devices Meeting*, IEEE Piscataway, NJ, USA **2011**, https://doi.org/10.1109/IEDM.2011.6131650.
[13] T. Heisig, J. Kler, H. C. Du, C. Baeumer, F. Hensling, M. Glss, M. Moors, A. Locatelli, T. O. Mentes, F. Genuzio, J. Mayer, R. A. De Souza, R. Dittmann, *Adv. Funct. Mater.* **2020**, *30*, 2004118.
[14] C. Baeumer, R. Valenta, C. Schmitz, A. Locatelli, T. O. Mentes, S. P. Rogers, A. Sala, N. Raab, S. Nemsak, M. Shim, C. M. Schneider, S. Menzel, R. Waser, R. Dittmann, *ACS Nano* **2017**, *11*, 6921.
[15] Q. Liu, S. B. Long, H. B. Lv, W. Wang, J. B. Niu, Z. L. Huo, J. N. Chen, M. Liu, *ACS Nano* **2010**, *4*, 6162.
[16] C. Lee, I. Kim, H. Shin, S. Kim, J. Cho, *Nanotechnology* **2010**, *21*, 7.
[17] N. Raab, D. O. Schmidt, H. C. Du, M. Kruth, U. Simon, R. Dittmann, *Nanomaterials* **2018**, *8*, 869.
[18] K. Y. Shin, Y. Kim, F. V. Antolinez, J. S. Ha, S. S. Lee, J. H. Park, *Adv. Electron. Mater.* **2016**, *2*, 1600233.
[19] J. Lee, C. Du, K. Sun, E. Kioupakis, W. D. Lu, *Acs Nano* **2016**, *10*, 3571.
[20] S. Choi, S. H. Tan, Z. F. Li, Y. Kim, C. Choi, P. Y. Chen, H. Yeon, S. M. Yu, J. Kim, *Nat. Mater.* **2018**, *17*, 335.

© 2021 The Authors. physica status solidi (RRL) Rapid Research Letters published by Wiley-VCH GmbH

[21] P. Badica, A. Agostino, M. M. R. Khan, S. Cagliero, C. Plapcianu, L. Pastero, M. Truccato, Y. Hayasaka, G. Jakob, *Supercond. Sci. Technol.* **2012**, *25*, 105003.
[22] S. Cagliero, E. Borfecchia, L. Mino, L. Calore, F. Bertolotti, G. Martinez-Criado, L. Operti, A. Agostino, M. Truccato, P. Badica, C. Lamberti, *Supercond. Sci. Technol.* **2012**, *25*, 125002.
[23] L. Gozzelino, R. Gerbaldo, G. Ghigo, F. Laviano, M. Truccato, *J. Supercond. Novel Mag.* **2017**, *30*, 749.
[24] L. Mino, V. Bonino, A. Agostino, C. Prestipino, E. Borfecchia, C. Lamberti, L. Operti, M. Fretto, N. De Leo, M. Truccato, *Sci. Rep.* **2017**, *7*, 9066.
[25] L. Mino, E. Borfecchia, A. Agostino, C. Lamberti, M. Truccato, *J. Electron Spectrosc. Rel. Phen.* **2017**, *220*, 69.
[26] A. Pagliero, L. Mino, E. Borfecchia, M. Truccato, A. Agostino, L. Pascale, E. Enrico, N. De Leo, C. Lamberti, G. Martinez-Criado, *Nano Lett.* **2014**, *14*, 1583.
[27] C. Plapcianu, A. Agostino, P. Badica, G. V. Aldica, E. Bonometti, G. Ieluzzi, S. Popa, M. Truccato, S. Cagliero, Y. Sakka, O. Vasylkiv, R. Vidu, *Ind. Eng. Chem. Res.* **2012**, *51*, 11005.
[28] V. Bonino, A., Agostino, C. Prestipino, O. Hernandez, M. Fretto, L. Mino, M. Truccato, *Crystengcomm* **2018**, *20*, 6667.
[29] M. W. Rabbani, V. Bonino, L. Spessa, A. Agostino, N. De Leo, C. Prestipino, M. Truccato, *Cryst. Growth Des.* **2021**, *21*, 3299.
[30] D. Torsello, L. Mino, V. Bonino, A. Agostino, L. Operti, E. Borfecchia, E. Vittone, C. Lamberti, M. Truccato, *Phys. Rev. Mater.* **2018**, *2*, 014801.
[31] M. Truccato, A. Agostino, E. Borfecchia, L. Mino, E. Cara, A. Pagliero, N. Adhlakha, L. Pascale, L. Operti, E. Enrico, N. De Leo, M. Fretto, G. Martinez-Criado, C. Lamberti, *Nano Lett.* **2016**, *16*, 1669.
[32] V. Bonino, D. Torsello, C. Prestipino, L. Mino, M. Truccato, *J. Synchr. Radiat.* **2020**, *27*, 1662.
[33] N. Medvedev, *J. Phys. Condens. Matter* **2020**, *32*, 435401.
[34] N. Medvedev, Z. J. Fang, C. Y. Xia, Z. Li, *Phys. Rev. B* **2019**, *99*, 144101.
[35] N. Medvedev, I. Milov, *Sci. Rep.* **2020**, *10*, 12775.
[36] R. A. Voronkov, N. Medvedev, A. E. Volkov, *Phys. Status Solidi RRL* **2020**, *14*, 1900641.
[37] S. H. Chang, J. Kim, C. Phatak, K. D'Aquila, S. K. Kim, J. Kim, S. J. Song, C. S. Hwang, J. A. Eastman, J. W. Freeland, S. Hong, *ACS Nano* **2014**, *8*, 1584.
[38] L. Mino, V. Bonino, F. Picollo, M. Fretto, A. Agostino, M. Truccato, *Adv. Electron. Mater.* **2019**, *5*, 1900129.
[39] P. Kofstad, *Nonstoichiometry, Diffusion, and Electrical Conductivity in Binary Metal Oxides*, Wiley-Interscience, New York **1972**.
[40] D. Y. Cho, M. Luebben, S. Wiefels, K. S. Lee, I. Valov, *ACS Appl. Mater. Interfaces* **2017**, *9*, 19287.
[41] R. Waser, R. Dittmann, G. Staikov, K. Szot, *Adv. Mater.* **2009**, *21*, 2632.
[42] G. Martinez-Criado, J. Villanova, R. Tucoulou, D. Salomon, J. P. Suuronen, S. Laboure, C. Guilloud, V. Valls, R. Barrett, E. Gagliardini, Y. Dabin, R. Baker, S. Bohic, C. Cohen, J. Morse, *J. Synchrotron Rad.* **2016**, *23*, 344.
[43] V. A. Sole, E. Papillon, M. Cotte, P. Walter, J. Susini, *Spectrochim. Acta, Part B* **2007**, *62*, 63.
[44] M. Gallart, T. Cottineau, B. Honerlage, V. Keller, N. Keller, P. Gilliot, *J. Appl. Phys.* **2018**, *124*, 133104.
[45] D. K. Pallotti, L. Passoni, P. Maddalena, F. Di Fonzo, S. Lettieri, *J. Phys. Chem. C* **2017**, *121*, 9011.
[46] X. L. Wang, Z. C. Feng, J. Y. Shi, G. Q. Jia, S. A. Shen, J. Zhou, C. Li, *Phys. Chem. Chem. Phys.* **2010**, *12*, 7083.
[47] A. Morales-Garcia, O. Lamiel-Garcia, R. Valero, F. Illas, *J. Phys. Chem. C* **2018**, *122*, 2413.
[48] A. Fissell, M. Czernohorsky, R. Dargis, H. J. Osten, *Mater. Sci. Forum* **2007**, *556–557*, 655.
[49] M. R. Hummon, A. J. Stollenwerk, V. Narayanamurti, P. O. Anikeeva, M. J. Panzer, V. Wood, V. Bulovic, *Phys. Rev. B* **2010**, *81*, 115439.
[50] C. La Torre, A. Kindsmuller, D. J. Wouters, C. E. Graves, G. A. Gibson, J. P. Strachan, R. S. Williams, R. Waser, S. Menzel, *Nanoscale* **2017**, *9*, 14414.
[51] Y. Dang, A. R. West, *J. Am. Ceram. Soc.* **2019**, *102*, 251.
[52] K. M. Kim, B. J. Choi, Y. C. Shin, S. Choi, C. S. Hwang, *Appl. Phys. Lett.* **2007**, *91*, 012907.
[53] K. M. Kim, D. S. Jeong, C. S. Hwang, *Nanotechnology* **2011**, *22*, 254002.
[54] K. C. Tang, A. C. Meng, F. Hui, Y. Shi, T. Petach, C. Hitzman, A. L. Koh, D. Goldhaber-Gordon, M. Lanza, P. C. McIntyre, *Nano Lett.* **2017**, *17*, 4390.
[55] J. Bonkerud, C. Zimmermann, F. Herklotz, P. M. Weiser, C. Seiffert, E. F. Verhoeven, L. Vines, E. V. Monakhov, *Semicond. Sci. Technol.* **2021**, *36*, 014006.
[56] C. Baeumer, C. Funck, A. Locatelli, T. O. Mentes, F. Genuzio, T. Heisig, F. Hensling, N. Raab, C. M. Schneider, S. Menzel, R. Waser, R. Dittmann, *Nano Lett.* **2019**, *19*, 54.

© 2021 The Authors. physica status solidi (RRL) Rapid Research Letters published by Wiley-VCH GmbH